ASTFE
American Society
of Thermal and Fluids Engineers

10th Thermal and Fluids Engineering Conference (TFEC)
March, 9-12, 2025
Partially Online Virtual and at George Washington University, DC, USA

TFEC-2025-56057

COMBINED STREAMWISE/STREAMLINE PRESSURE GRADIENT EFFECTS ON TURBULENT WALL-BOUNDED FLOWS WITH PASSIVE SCALAR TRANSPORT

David Paeres,* Subhajit Roy, Matthew Holland, Guillermo Araya

Computational Turbulence and Visualization Lab., Department of Mechanical Engineering, University of Texas at San Antonio, TX 78249, USA. https://ceid.utsa.edu/garaya/

ABSTRACT

Streamwise flow acceleration and deceleration is investigated over incompressible spatially-developing turbulent boundary layers (SDTBL) subject to the combined effects of streamwise/streamline pressure gradient (i.e. a two-dimensional curved hill under zero, adverse and favorable external pressure gradient). The selected numerical tool is RANS (Reynolds-Averaged Navier-Stokes) plus two eddy-viscosity models: the $K-\omega$ SST (henceforth SST) and the Spalart-Allmaras (henceforth SA) turbulence models. The evolution of three passive scalars is also scrutinized using the following molecular Prandtl or Schmidt numbers, Pr = 0.2, 0.71, and 2. The complex geometry (2D curved hill), as in Baskaran et al. (1987), has been reproduced and validated in our previous studies, Paeres et al. (2022a,b). The combined strong adverse/favorable streamline curvature-driven pressure gradient caused by concave/convex surface curvatures implied a horizontal ceiling in wind tunnel experiments by Baskaran et al. (1987). In the present study, the effects of streamwise pressure gradient are evaluated by manipulating the top surface of the RANS computational domain: zero-pressure gradient, divergent and convergent top-wall cases. Both turbulence models have been consistent in the outcomes, except downstream of the curved hill. It is observed that the SST model predicts slightly longer reattachment lengths than the SA model, and stronger reversal flows. Furthermore, the presence of an external streamwise pressure gradient does not affect the separation bubble length itself, but it does affect C_f peaks, having the top-diverging wall case the largest impact. The presence of strong streamwise/streamline pressure gradients breaks down the Reynolds analogy between the momentum and passive scalar fields.

KEY WORDS: Keywords: RANS, passive scalar, streamwise pressure gradient, concave/convex curvature, turbulent boundary layer.

1. INTRODUCTION

Flow separation at high Reynolds numbers is one of the most challenging types of turbulent flows, and still remains one of the major unresolved problems of fluid dynamics, according to Williams (1977). Simpson (1989), in his well-known review of turbulent boundary layer separation, claimed *"the effects of significant wall curvature are not well described quantitatively, although most separation cases occur on curved wall."* According to Patrick (1987), more reliable data and large-scale models are required to better define the turbulence structure of the backflow region in very strong streamwise Adverse Pressure Gradient (APG), which is responsible for boundary layer detachment. In the case of incompressible turbulent flow over a curved hill, separation zones will occur due to the Adverse Pressure Gradient (APG) or flow deceleration caused by the

*Corresponding David Paeres: david.paerescastano@utsa.edu

NOMENCLATURE

$()_e$	Parameter at the boundary layer edge
$()_{(P)}$	Parameter in function of pressure gradient
$()_w$	Parameter at the wall
APG	Adverse Pressure Gradient
β	Pressure Parameter of Clauser
C_f	Skin friction coefficient, $2 * (u_\tau/u_e)^2$
ΔP	Pressure Parameter of Patel
δ	Boundary Layer
δ^*	Displacement Thickness
δ_t	Thermal Boundary Layer
FPG	Favorable Pressure Gradient
$K_{(P)}$	Pressure Parameter of Launder
ν	Molecular kinematic viscosity
P	Static Pressure
Pr	Molecular Prandtl number
RANS	Reynolds-Averaged Navier-Stokes
Re_θ	Momentum Thickness Reynolds Number
ρ	Density
SA	Spalart Allmaras turbulent model
SDTBL	Spatially-developing turbulent boundary layer
SST	Shear Stress Transport $K-\omega$ turbulent model
τ	Shear Stress
u_τ	Skin friction velocity, $\sqrt{\tau_w/\rho}$
U	Velocity
x	Cartesian Coordinate (x=0 is the hill top)
ZPG	Zero Pressure Gradient

presence of convex wall curvature. In spite of the significant progress performed in the last twenty years, modeling efforts for separated flows have been hindered due to the lack of information on the mechanisms that control the separation of the boundary layer by large-scale structures. *Furthermore, how passive scalar transport behaves under this condition also remains unknown*. The turbulent transport of passive scalars is crucial in many industrial applications of technological importance, such as in turbine-blade film cooling, heat transfer in electronic/mechanical devices, chemicals dissolved in gases, and contaminant/humidity dispersed in atmospheric flow, to name a few. Furthermore, a passive scalar is defined as a diffusive contaminant that exists in such a low concentration in a flow that it has no effect on the dynamics of the fluid motion, Warhaft (2000). However, that low concentration of passive scalar is sufficient to cause a significant impact on energy expenditures, air pollution, and the design of chemical processes. The transport phenomenon in real-situation flows usually occurs under complicated external conditions, such as pressure gradients, favorable (FPG) and adverse (APG), complex geometry (concave/convex surface), high Reynolds numbers, and spatially-developing turbulent boundary layers (SDTBL). The consideration of temperature is performed based on the theory of passive scalar transport as in Li et al. (2009). Furthermore, the separation of boundary layer flow, attributed to the presence of a sufficiently strong Adverse Pressure Gradient (APG), represents by far the most undesirable situation in the momentum/scalar transport. The boundary layer parameters experience sudden changes due to an abrupt thickening of the rotational flow region or backflow close to the wall (Simpson (1989)), which may cause a critical reduction in the performance of the device (e.g., pressure drag increase in airfoils or heat transfer decrease in turbine blades). For this reason, flow separation has been the topic of several theoretical, experimental, and numerical studies in the past few decades (Simpson (1985); Simpson et al. (1987)), however, there is still some "terra ignota". In the present manuscript, the influence of combined streamwise-streamline and isolated streamline pressure gradients on the momentum and passive scalar transport is explored via two turbulence closure models (SA and SST) for Reynolds shear stresses and the simple, but robust, turbulent Prandtl number for wall-normal turbulent heat flux modeling. The incoming turbulent flow conditions (upstream of the curved hill) are validated by DNS database from Lagares and Araya (2021).

2. GOVERNING EQUATIONS AND BOUNDARY CONDITIONS

The 2D curved hill under consideration is a reproduction of the experiments described by Baskaran et al. (1987). The scenario involves an incoming horizontal airstream at 20 m/s passing over a simple curved protuberance of 1.284 m long with a radius, R, of 1.08 m. The protuberance's entrance and exit had concave surfaces of -0.40 m and -0.48 m of radius, respectively. Therefore, the normalized curvature ratios, δ_{ref}/R,

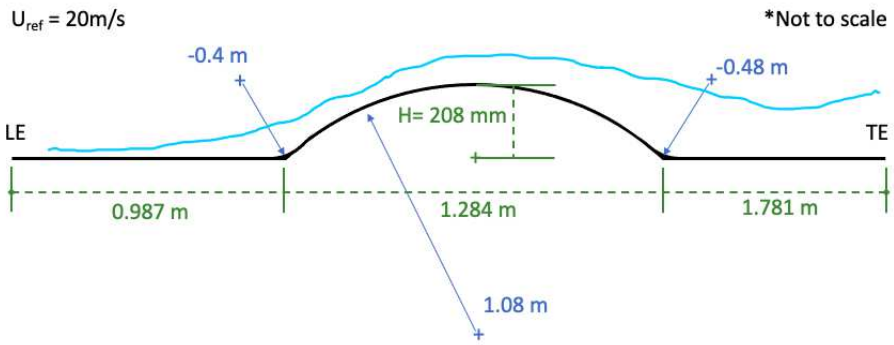

Fig. 1 Curved hill diagram. From Paeres et al. (2022a,b); reprinted by permission of the American Institute of Aeronautics and Astronautics, Inc.

are as follows: 0.037, -0.1, and -0.083 for the convex (positive) and the concave (negative) wall curvatures, where δ_{ref} is the reference boundary layer thickness taken at the beginning of the curved hill. Figure 1 shows an example of the geometry, which has already been validated in our previous studies Paeres et al. (2022a,b). We are keeping the selected numerical tool RANS (Reynolds-Averaged Navier-Stokes) plus the two eddy-viscosity models: the $K-\omega$ SST (henceforth SST) and the Spalart-Allmaras (henceforth SA) turbulence models. Readers are referred to Paeres et al. (2022b) for a comprehensive description of the governing equation and turbulence transport approach. In addition to studying the effects of the streamwise pressure gradient by manipulating the top surface of the RANS computational domain, this study also ventures to delve into the effect of several molecular Prandtl numbers. These are analyzed using the following molecular Prandtl numbers: Pr = 0.2, 0.71, and 2, with their respective turbulent Prandtl numbers: 0.52, 0.87, and 1.319, respectively.

For the conducted analysis, it is essential to utilize curvilinear coordinates. This approach allows for a more accurate representation of the physical phenomena occurring along the complex geometries of the wall surfaces. The freestream flow parameters are defined at the edge of the turbulent boundary layer (e.g., U_e, P_e, T_e, etc.), which is more appropriate for flows over wall curvatures. Consequently, the equations governing fluid dynamics must be derived in curvilinear coordinates to capture the nuances of the flow behavior accurately. The following elaborates on the derivation of these equations within the curvilinear coordinate framework, highlighting the necessity of this approach for our specific analysis. Taking Bernoulli's equation 1:

$$P+\frac{\rho {U_e}^2}{2}+\rho g h=\text{const.} \tag{1}$$

where P is static fluid pressure, U_e is the freestream velocity, ρ is the fluid density, g is the acceleration due to gravity, and h is the elevation of the point. Considering s as the streamwise coordinate, differentiating eq. 1 by s gives:

$$\frac{\partial P}{\partial s}+\rho U_e\frac{\partial U_e}{\partial s}+\rho g\frac{\partial h}{\partial s}=0\longrightarrow\frac{\partial U_e}{\partial s}=-\left(\frac{1}{\rho U_e}\frac{\partial P}{\partial s}+\frac{g}{U_e}\frac{\partial h}{\partial s}\right)\longrightarrow\frac{\partial U_e}{\partial s}=-\left(\frac{1}{\rho U_e}\frac{\partial P}{\partial s}+\frac{g}{U_e}\frac{\partial h}{\partial s}\right) \tag{2}$$

$$\text{And neglecting potential energy due to elevation, } \frac{\partial h}{\partial s}\approx 0\longrightarrow\boxed{\frac{\partial U_e}{\partial s}=\frac{-1}{\rho U_e}\frac{\partial P}{\partial s}} \tag{3}$$

The following dimensionless pressure parameters are used in this study to evaluate the strengths of combined streamwise/streamline pressure gradients. Launder (1965), where U_∞ is freestream velocity and ν is the

kinematic viscosity. As streamwise notation and function of pressure gradient at boundary layer edge:

$$K = \left(\frac{\nu}{{U_\infty}^2}\right)\frac{\partial U_\infty}{\partial x} \longrightarrow \boxed{K_{(P)} = \left(\frac{-\nu}{\rho {U_e}^3}\right)\frac{\partial P_e}{\partial s}} \tag{4}$$

Patel (1965) defined a dimensionless pressure parameter based on the friction velocity, u_τ. For our case, we can rewrite Patel's equation as follows but note the high similarity between Launder and Patel when both parameters are expressed in function of pressure gradient (i.e., Equations 4 and 5). Both parameters are a streamwise pressure gradient multiplied by a factor of viscosity over a cubed velocity. Recalling that wall-shear stress is density times squared skin friction velocity.

$$\Delta P = \left(\frac{\nu}{\rho {u_\tau}^3}\right)\frac{\partial P}{\partial x} \longrightarrow \boxed{\Delta P = \left(\frac{\nu}{\rho {u_\tau}^3}\right)\frac{\partial P_e}{\partial s}} \tag{5}$$

The Clauser's parameter β (Clauser (1954, 1956)) is defined as follows, where δ^* is the displacement thickness and τ_w is the wall shear stress.

$$\beta = \left(\frac{\delta^*}{\tau_w}\right)\frac{\partial P}{\partial x} \longrightarrow \boxed{\beta = \left(\frac{\delta^*}{\rho u_\tau^2}\right)\frac{\partial P_e}{\partial s}} \tag{6}$$

3. COMPUTATIONAL DOMAIN AND MESH DESIGN

We are evaluating the effect of different streamwise pressure gradients over a curved hill by manipulating the top surface, i.e. ZPG, APG, and FPG. In an earlier study (Paeres et al. (2022b)), the top surface was horizontal, mimicking the wind-tunnel geometry as in Baskaran et al. (1987). Previously, we utilized three different meshes which we labeled as coarse, medium, and fine. For all of them, recycled and validated inlet profiles of velocity and temperature were incorporated to bypass unrealistic freestream inlet profiles and to avoid an extensive inlet developing section. In the current work, we employed a similar grid point distribution as the fine mesh case in Paeres et al. (2022b) according to the acquired knowledge from the grid independence test process. The obtained mesh was considered as the baseline and we modified the upper boundary. The objective is to assess the impact of streamwise pressure gradient by adjusting the upper surface of the RANS computational domain. Consistent with our objectives, the present study investigates three additional "cases" which we denote as *ZPG* for a constant top-to-floor distance, *FPG* for a convergent top-wall with a ceiling inclined at -2^o, and *APG* for a divergent top-wall with a ceiling inclined at 10^o. The ceiling inclination degrees are relative to the horizontal and these values were chosen following as reference the work of Driver and Seegmiller (1985). Additionally, a small adjustment was made to the new meshes, ensuring that the vertical cell distribution was independent of the ceiling height, providing identical near-wall resolution across cases. Figure 2 illustrates the three new meshes according to these cases.

4. RELEVANT RESULTS AND DISCUSSION

In this section, we are showing and discussing RANS results on the effect of the combined streamwise/streamline pressure gradient over the momentum and passive scalar boundary layer. The boundary layer thickness δ vs. x/δ_{ref}, is exhibited by fig. 3(a). Based on the figure, δ_{ref} = 0.04m was selected, as all solutions converge to this value before the boundary layer thickness begins to shrink. The incoming ZPG turbulent boundary layer shows an almost linear growing trend, which is further affected by the presence of APG (-30 $< x/\delta_{ref} <$ -20) since the flow decelerates due to the presence of the curved hill. Therefore, it can be observed a thickening process of the boundary layer in the region -30 $< x/\delta_{ref} <$ -20, followed by a sharp shrink within a very short distance (-20 $< x/\delta_{ref} <$ -15) caused by the very strong FPGs due to the first concave curvature in all cases.

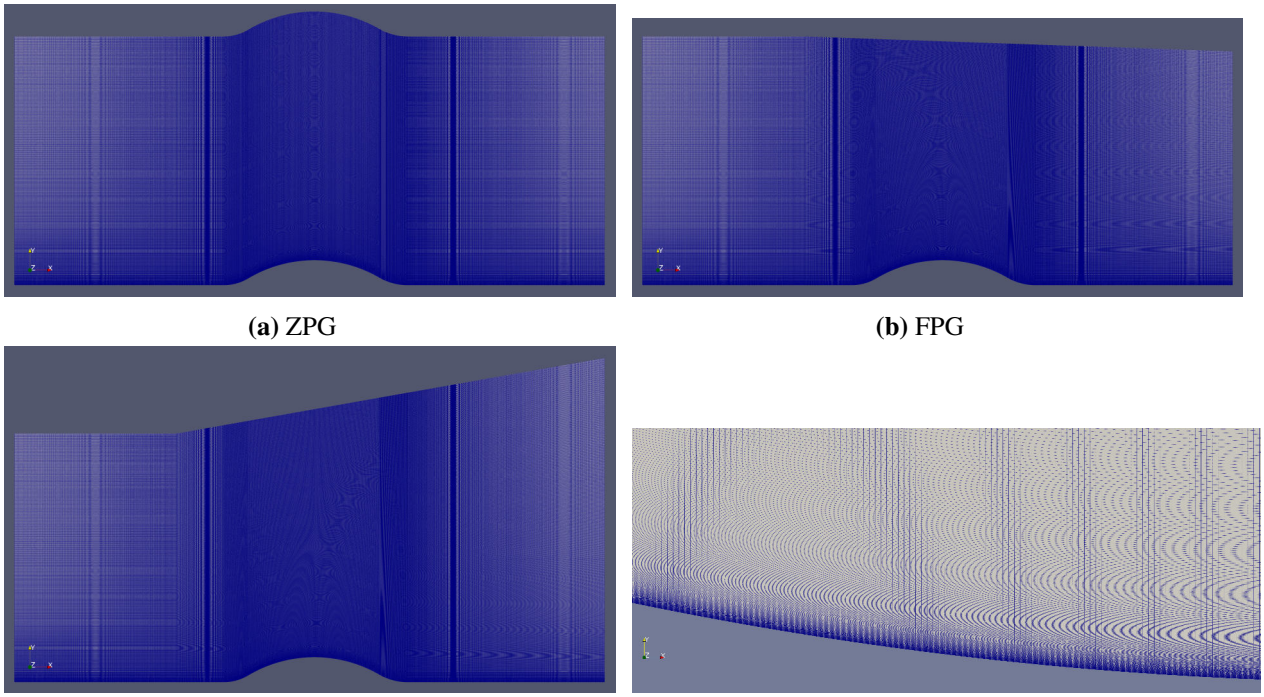

(a) ZPG **(b)** FPG

(c) APG **(d)** Near wall region close-up

Fig. 2 Schematic of the mesh configurations: (a) ZPG, (b) FPG, (c) APG, and (d) near wall region close-up at the second concave surface.

The recovery process (growth) of δ seems to be faster under a top-converging ceiling (i.e., external FPG case) along the convex wall curvature. Peak values of δ can be observed around $x/\delta_{ref} \approx 20$, by the end of the second concave curvature. Downstream of the curved hill in the flat section, there is a very strong decrease in the boundary layer thickness for the top-diverging wall (streamwise APG). Overall and so far, both turbulence models have been highly consistent in their outcomes, except in the second flat region located downstream of the curved hill. The physics explanation could be linked to the severe flow distortion infringed on the incoming turbulent boundary layer due to the combined streamwise/streamline pressure gradient effects, significantly impacting the downstream boundary layer development. Figure 3(b) depicts the streamwise development of the flow velocity at the boundary layer edge, U_e, for the external imposed streamwise pressure gradients, i.e. ZPG, FPG, and APG. The variation of the freestream flow velocity clearly indicates the local edge pressure gradient zones: the boundary layer undergoes an initial ZPG up to $x/\delta_{ref} \approx$ -40, later a strong APG (flow deceleration) up to the middle of the first concave region, a very strong FPG up to the hilltop followed by a very strong APG (and flow separation) up to the middle of the second concave region, and finally starts recovering in the end part of the concave surface and beyond (presence of FPG or flow acceleration). Interestingly, while external ZPG and FPG cases achieve similar values of the incoming freestream velocity, the APG case shows lower values (approximately 20% lower). This is the reason for the strong shrinking process observed on the δ profile in fig.3(a). Figure 4(a) shows the streamwise development of the skin friction coefficient, C_f. As expected, the local wall shear stresses experience decreases and increases in agreement with the local edge pressure gradient, as shown in Fig. 4(b). At the end of the convex zone, just before the second concave section, C_f reaches a value of zero, indicating the potential location of the flow separation point over the curved hill. The major conclusions regarding the separation flow bubble are threefold: (i) the SST model predicts slightly longer lengths for reattachment and stronger reversal flows, as evidenced by the high (negative) C_f values, (ii) the presence of an external streamwise pressure gradient does not seem to significantly affect the length of the separation bubble; and (iii) the APG ceiling case tends to show largest absolute values of the skin friction coefficient throughout the domain; however, local C_f values are notably larger in the APG case regarding the other two cases (i.e., ZPG and FPG) downstream of the separation bubble. This is understandable considering

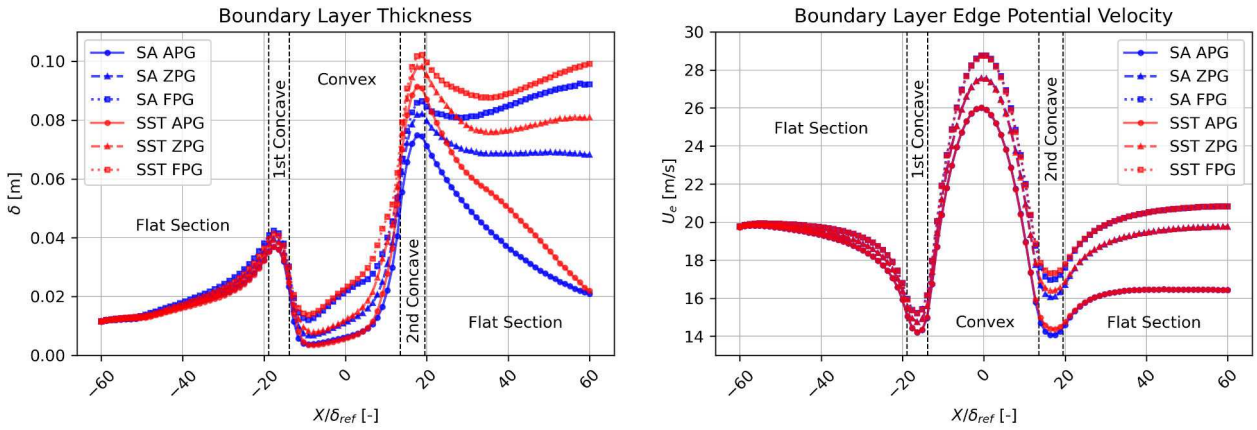

(a) **(b)**

Fig. 3 (a) Height of boundary layer, and (b) Velocity at the edge of boundary layer. Blue line for SA model and red line for SST model. Cases identified by symbols: APG with (●), ZPG with (▲), and FPG with (■).

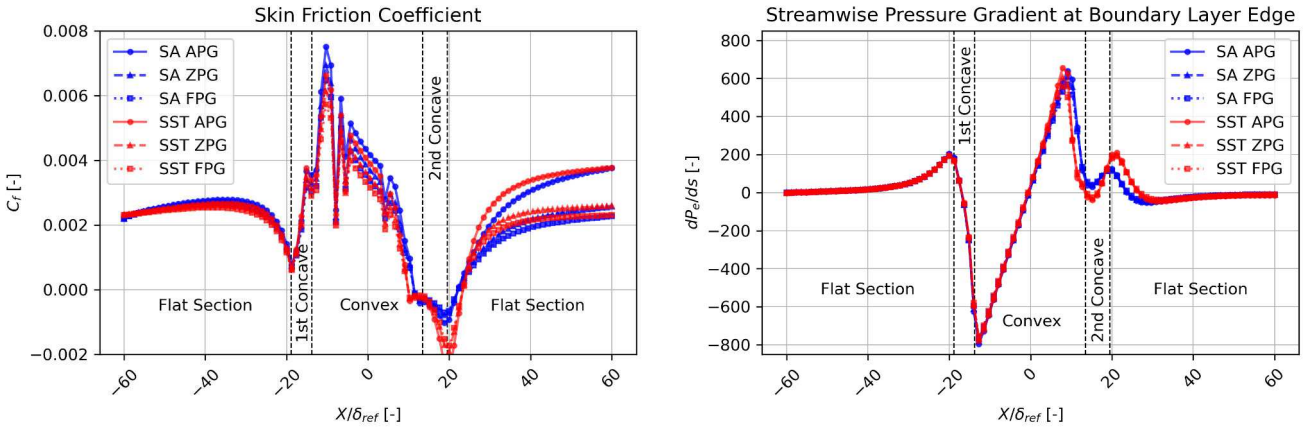

(a) **(b)**

Fig. 4 (a) Skin friction coefficient, and (b) Streamwise Pressure Gradient at edge of boundary layer. Blue line for SA model and red line for SST model. Cases identified by symbols: APG with (●), ZPG with (▲), and FPG with (■).

the relatively large inclination angle infringed on the ceiling. The edge pressure gradient is exhibited by Fig. 4(b). The different pressure gradients and their strengths are clearly observed: ZPG (-60 $< x/\delta_{ref} <$ -40), moderate APG (-40 $\leq x/\delta_{ref} <$ -20), strong FPG (1^{st} concave region), strong APG (convex region, mostly), strong FPG (from $x/\delta_{ref} \approx 10$ to the beginning of the 2^{nd} concave region), moderate APG (within the 2^{nd} concave region), moderate FPG (20 $< x/\delta_{ref} <$ 30), and ZPG for $x/\delta_{ref} \geq 30$. It is worth highlighting the almost linear increasing trend of the edge pressure gradient in the convex region of the curved hill. Also, note that the APG peak does not occur at the convex zone end but slightly earlier.

Fig. 5 draws a comparison between the different pressure gradients and turbulence models for the displacement thickness, δ^*, and the momentum thickness Reynolds number, Re_θ. Clearly, there is a strong effect of the pressure gradient on the momentum thickness, θ, as seen in Fig. 5(b) that persists beyond the immediate region of the curve. This is consistent with the boundary layer thickness, δ, trend seen in Fig. 3(a). However, this trend is not seen in the displacement thickness data, δ^*, as shown by 5(a). In the case of δ^*, the effects of the curved surface are limited to the region immediately around it, and the flow trend following the surface appears almost unaffected by the presence of the disruption. Additionally, there is no significant deviation in

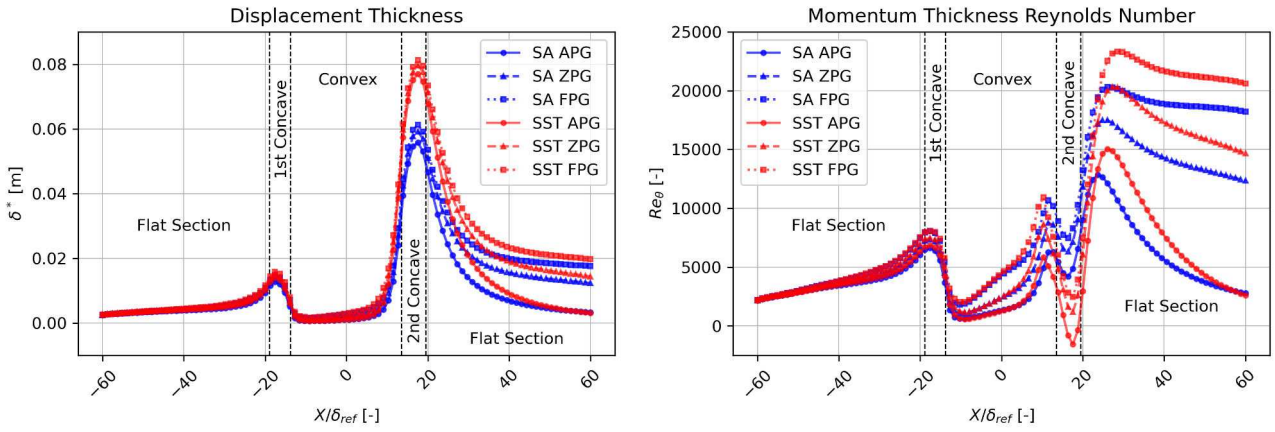

Fig. 5 (a) Displacement Thickness (δ^*), and (b) Momentum Thickness Reynolds Number (Re_θ). Blue line for SA model and red line for SST model. Cases identified by symbols: APG with (●), ZPG with (▲), and FPG with (■).

the results of the turbulence models until the flow reaches the back side of the curved surface. At this point, δ^* experiences a drastic difference in the size of the displacement boundary layer, which would indicate that the two turbulence models cannot agree where the edge of the boundary layer should lie for the potential flow for this region, which is present in Fig. 3(b) to a dampened extent. However, the two models then do converge towards the displacement boundary layer thickness as it reaches a new freestream condition. There is a similar trend with Re_θ, where turbulence models do not agree on the thickness of the momentum boundary layer. Unlike with δ^*, the SA model overpredicts Re_θ profiles relative to the SST model in the controversial flow separation bubble, which indicates that the two turbulence models do not agree to the shape of the boundary layer under this condition. Also unlike with δ^*, except for the adverse pressure gradient condition, the two models do not converge to the new freestream trend. It is interesting that both models do converge to a freestream trend for the APG condition, as one would think that this could be a weaker point for both models.

Figure 6 and 7 illustrates the alignment and divergence between the pressure gradient ceiling conditions and turbulence models on pressure gradient parameters, appearing more starkly than the trends of the previous and traditional flow parameters. The pressure gradient conditions result in a variation of the peak values for the Launder parameter ($K_{(P)}$), as shown in Fig. 6(a). All cases exhibit consistent trends and comparable values overall. Even during the transition of $K_{(P)}$ values, from negative to positive in the first concave region, and from positive to negative in the convex region, the pressure gradient parameters follow a similar behavior based on SA and SST turbulence models. Beyond the flow separation point ($x/\delta_{ref} \approx 10$), a divergence in the magnitude of the lowest negative values occurs for all cases. This is consistent with the trends that are illustrated previously in this section, where the SA and SST models deviate from one another on the back side of the curved surface. The SA model also returns to a new freestream condition sooner than the SST model does. These behaviors are also seen in the Patel parameter (ΔP), shown in Fig. 6(b). While the peak and trough in the first concave section are not prominent, the peaks and troughs following the convex section become more pronounced. This could be attributed to ΔP using the skin friction velocity cubed; as the velocity approaches zero, it leads to a very small division factor, explaining the pronounced and off-scale values. The most noticeable differences in the trend of the Patel parameter stem from the two different turbulence models. It is not coincidental that the SA model predicts more extreme peaks and troughs compared to the SST model. As seen in Fig. 4(a), the SA model consistently predicts lower C_f values (in magnitude) than the SST model in the second concave region most interesting differences in the trend of this parameter come from the two different turbulence models. The SA model makes the peaks and troughs highly dependent on the pressure

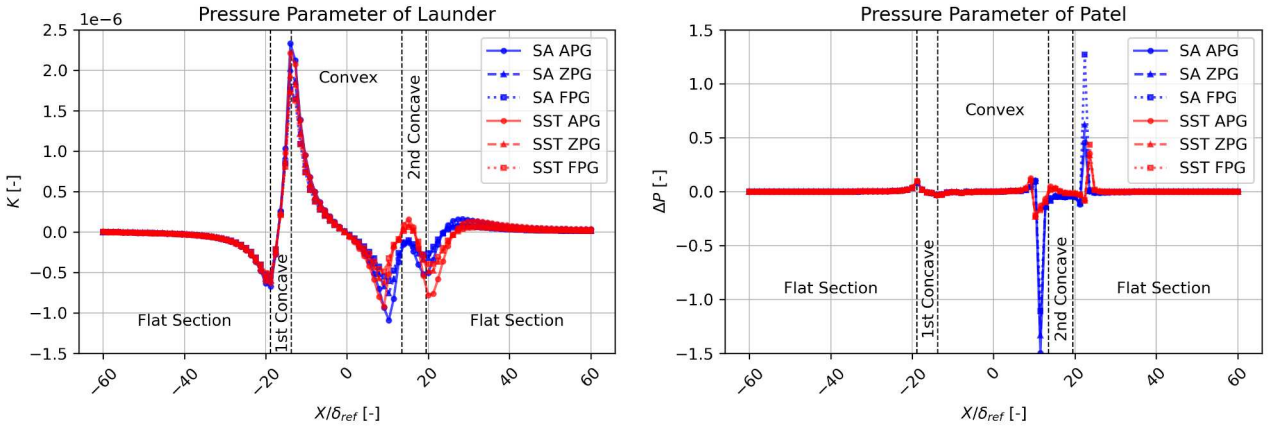

(a) **(b)**

Fig. 6 (a) Launder's Pressure Parameter ($K_{(P)}$), and (b) Patel's Pressure Parameter (ΔP). Blue line for SA model and red line for SST model. Cases identified by symbols: APG with (●), ZPG with (▲), and FPG with (■).

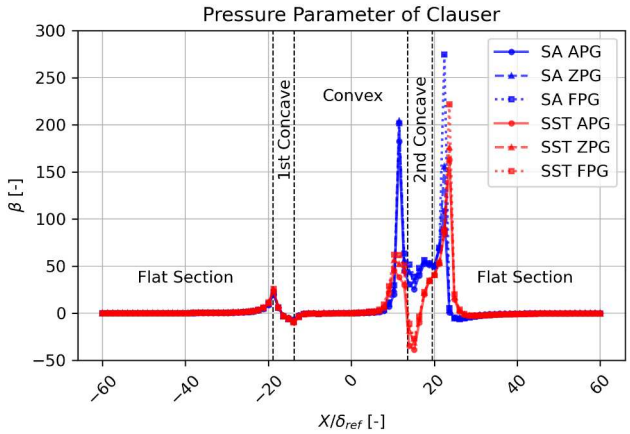

Fig. 7 Clauser's Pressure Parameter (β), blue line for SA model and red line for SST model. Cases identified by symbols: APG with (●), ZPG with (▲), and FPG with (■).

gradient, but not so much with the SST model, where the different pressure gradient conditions affect the Patel parameter peak value minimally. This would indicate that the SST model may not be as sensitive in local behaviors to freestream conditions as the SA model, whether or not this is correct to the exact or real behavior. Additionally, it is clear that the SA model lags the SST model in the negative values for the first large drop in the Patel parameter and precedes the SST model in the sharp peak. This may indicate that the SA model may be compensating for localized errors with larger trends.

Figure 7 shows the streamwise variation of Clauser's pressure parameter, β, along the curved hill using the SA and SST turbulence models. ZPG conditions are relatively flat across the surface for both models, indicating minimal impact on the boundary layer. Under APG conditions (near both concave sections), both models exhibit positive peaks in β around $x/\delta_{ref} \approx$ -20, 10, and 25. Since β also considers the wall shear stress, the peaks are more pronounced in the neighborhood of the second concave section, and once again, the SA model is the one with values almost off the chart. Furthermore, the SST turbulence model is well-known for its good performance in boundary layer flows subjected to APG, with eventual separation. Near the flow separation point (at the end of the convex section), the negative drop in β is solely dictated by dP_e/ds due to how equation 6 was applied. This means that if the sign of u_τ were considered, both turbulence models would switch signs, as u_τ is consistently negative in this region.

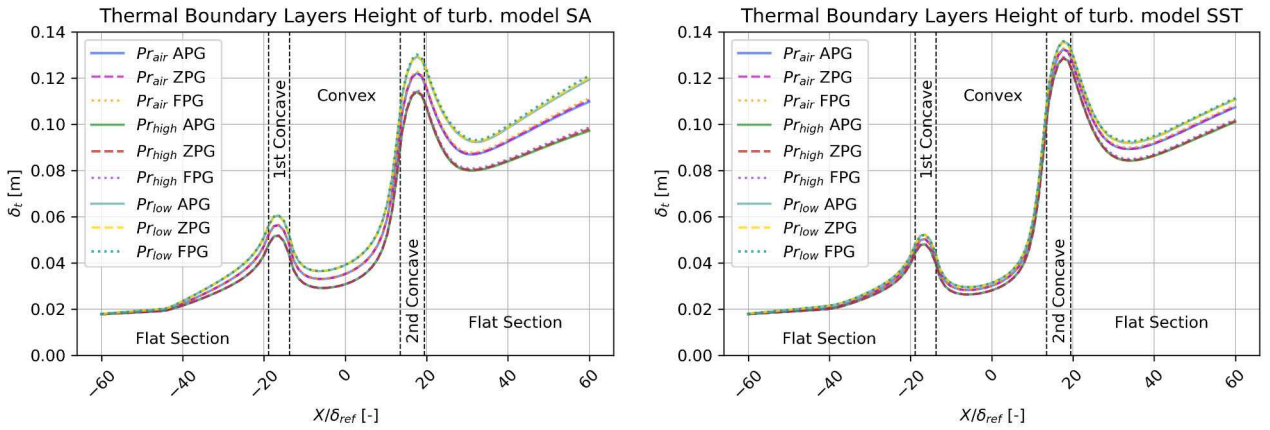

Fig. 8 Thermal boundary layer thickness for turbulent models: (a) SA, and (b) SST. Black line for Pr of air, yellow line for high Pr, and green line for low Pr. Cases identified by symbols: APG with (•), ZPG with (▲), and FPG with (■).

Figure 8 represents the streamwise distribution of thermal boundary layer thickness (δ_t), which is a measure of the distance over which the temperature gradient exists in the boundary layer, using the SA and SST models. In the present study, the temperature field is considered a passive scalar. The thermal boundary layer forms simultaneously with the momentum boundary layer, but the thickness depends on the thermal diffusivity of the fluid, which is governed by the Prandtl number (Pr) or better say, the Schmidt number (S_c). In both plots, δ_t is shown for three different Prandtl numbers ($Pr_{\text{air}} = 0.71, Pr_{\text{high}} = 2, Pr_{\text{low}} = 0.2$), across APG, ZPG, and FPG flow conditions. Higher Prandtl number indicates lower passive scalar diffusivity regarding the momentum diffusivity, resulting in a thinner passive scalar boundary layer. On the contrary, lower Prandtl number implies lower passive scalar diffusivity than that of the momentum field, which results in a thicker passive scalar boundary layer. Adverse pressure gradient cases show a significant increase in passive scalar boundary layer thickness for both turbulence models, particularly around $x/\delta_{ref} \approx 20$, corresponding to flow deceleration and eventual flow separation. On the other hand, ZPG cases exhibit a more steady and consistent boundary layer thickness (between turb. models). FPG cases show a marked decrease in thickness, particularly in the high-Pr cases, as the boundary layer thins with the accelerating flow. SST model (Fig. 8 (b)) shows more pronounced variations in thermal boundary layer thickness compared to the SA model, particularly in regions of internal strong pressure gradients (APG and FPG, or between peak values of concave zones). This suggests that the SST model, with its ability to more accurately capture near-wall turbulence, better resolves the interactions between the pressure gradients and the thermal boundary layer. This is especially important in engineering applications where accurate heat transfer predictions are critical, such as in turbomachinery and aerodynamics. In essence, all six cases predict that the thermal boundary layer thickness is approximately 0.1 m at the start of the second concave region. Additionally, before the separation bubble forms, for cases with the same Prandtl number (Pr), the differences in the predicted thermal boundary layer thickness due to changes in the external pressure gradient are well below 1%. However, once the influence of the separation bubble is present, the differences between these cases become slightly noticeable, although they do not exceed approximately 2%, which represents the maximum deviation observed. The largest difference occurred in the predictions using the SA turbulence model with the Pr_{low} when comparing the FPG and APG cases. Similarly, the SA model exhibited greater variations across its cases compared to those observed in the SST model. Generally, as expected, the thermal boundary layer height predictions followed a descending order of FPG $>$ ZPG $>$ APG. The only exception was the SST turbulence model with Pr_{low} between the ZPG and APG cases, where negative differences were observed in regions influenced by the separation bubble. Figure 9 shows iso-contours of streamwise velocity including some streamlines. The location of the separation bubbles is clearly visualized downstream of the hill. Whereas, the effects of the external streamwise pressure

gradients, by manipulating the top surface, on the separated flow area are not evident; it can be inferred that the SST model predicts a much larger zone for the bubble.

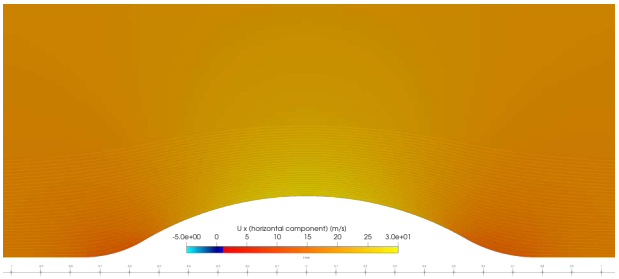

(a) U_x ZPG Potential

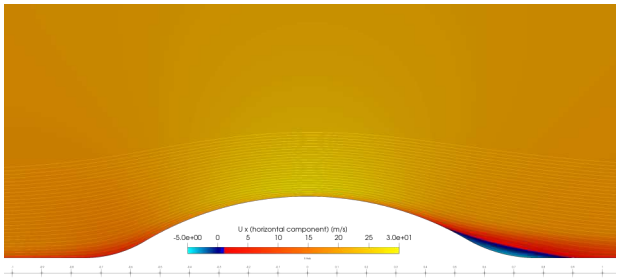

(b) U_x APG SA

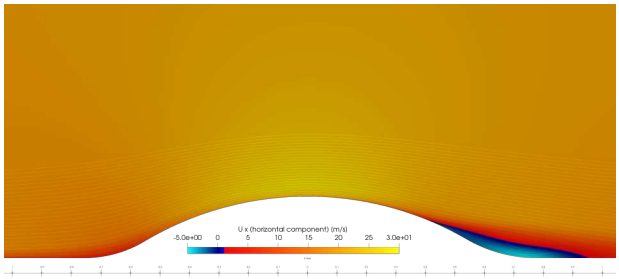

(c) U_x APG SST

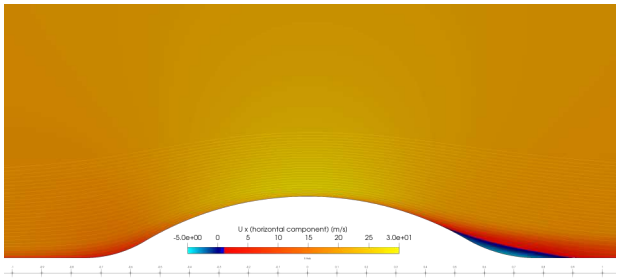

(d) U_x ZPG SA

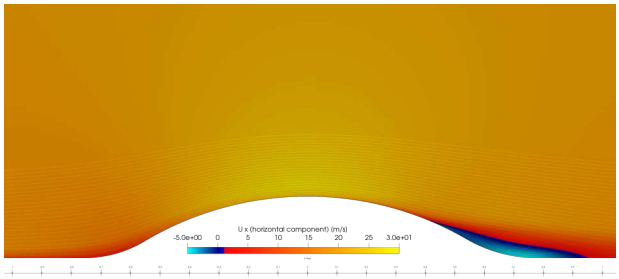

(e) U_x ZPG SST

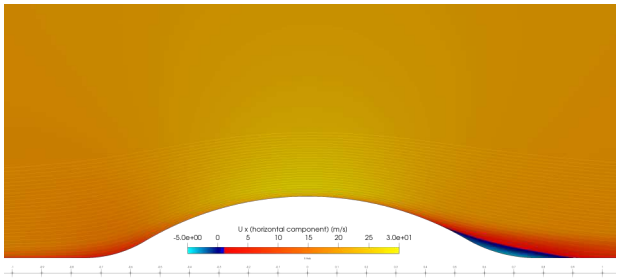

(f) U_x FPG SA

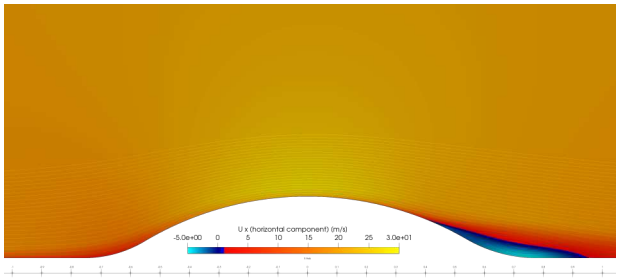

(g) U_x FPG SST

Fig. 9 Iso-contours of the horizontal velocity (U_x) presented by the external ceiling condition applied (i.e., APG, ZPG, and FPG) and by the turbulent model used (SA and SST). Prescription of some streamlines.

5. CONCLUSIONS

We perform a numerical study of a turbulent boundary layer and passive scalar transport subject to a curved hill and the combined effect of streamwise/streamline pressure gradient. The study was limited to a Reynolds Averaged Navier Stokes simulation (RANS) plus two eddy-viscosity turbulence models (i.e., SST and SA). The domain geometry was reproduced following work by Baskaran *et al.* Baskaran et al. (1987). The inlet

velocity components and temperature were recycled and re-injected from a precursor ZPG simulation to avoid a longer developing section and better control (and match with experiments) the incoming reference boundary layer parameters. Momentum and thermal turbulent boundary layers undergo severe distortions due to the combined effect of streamwise/streamline strong pressure gradients. Both turbulence models have been consistent in the outcomes, except in the second flat zone (downstream of the curved hill). It is hypothesized that the infringed changes on the turbulent boundary layer parameters by combined wall curvatures and external streamwise pressure gradients are responsible for result disparities by both turbulence models downstream of the hill. By far, the most important aspect of flow separation modeling is the ability of any turbulence model to characterize the reattachment length. It is concluded that the SST model predicts slightly longer reattachment lengths than the SA model, and stronger reversal flows given. Interestingly, the presence of an external streamwise pressure gradient seems not to affect the separation bubble length itself, but it does affect C_f peaks, having the APG case (top-diverging wall) the largest impact. In terms of the dimensionless pressure gradient parameters, the SST and SA generate highly similar values. However, there have been significant differences in the separation flow bubble, as expected. The streamwise development of the passive scalar boundary layer thickness has shown strong dissimilarities with the momentum boundary layer thickness caused by the presence of strong pressure gradients, which annihilate the Reynolds analogy.

ACKNOWLEDGMENTS

This material is based upon work supported by the National Science Foundation under grant #2314303 (CAREER). This material is based on research sponsored by the Air Force Office of Scientific Research (AFOSR) under agreement number #FA9550-23-1-0241.

REFERENCES

Baskaran, V., Smits, A., and Joubert, P., (1987) "A turbulent flow over a curved hill part 1. growth of an internal boundary layer," *Journal of Fluid Mechanics*, 182, pp. 47–83.

Clauser, F., (1954) "Turbulent boundary layers in adverse pressure gradients," *Journal of the Aeronautical Sciences*, 21(2), pp. 91–108. https://doi.org/10.2514/8.2938

Clauser, F. H., (1956) "The turbulent boundary layer," . vol. 4 of *Advances in Applied Mechanics*. Elsevier, pp. 1–51. https://www.sciencedirect.com/science/article/pii/S0065215608703703

Driver, D. and Seegmiller, H., (1985) "Features of a reattaching turbulent shear layer in divergent channel flow," *AIAA Journal*, 623(02).

Lagares, C. J. and Araya, G., (2021) "Compressibility effects on high-reynolds coherent structures via two-point correlations," *AIAA AVIATION 2021 FORUM*. https://arc.aiaa.org/doi/abs/10.2514/6.2021-2869

Launder, B. E., (1965) Laminarization of the turbulent boundry layer acceleration., PhD thesis, Massachusetts Institute of Technology.

Li, Q., Schlatter, P., Brandt, L., and Henningson, D. S., (2009) "Dns of a spatially developing turbulent boundary layer with passive scalar transport," *International Journal of Heat and Fluid Flow*, 30(5), pp. 916–929.

Paeres, D., Lagares, C., and Araya, G., (2022) "Assessment of incompressible turbulent flow over a curved hill with passive scalar transport," *AIAA SciTech, AIAA 2022-0049*.

Paeres, D., Lagares, C., and G., A., (2022) "Assessment of turbulence models over a curved hill flow with passive scalar transport," *Energies*, 15, pp. 6013.

Patel, V., (1965) "Calibration of the preston tube and limitation on its use in pressure gradients," *Journal of Fluid Mechanics*, 23, pp. 185–208.

Patrick, W. P., (1987) "Flowfield measurements in a separated and reattached flat plate turbulent boundary layer," *NASA*, CR4052.

Simpson, R., (1985) "Two-dimensional turbulent separated flow," *AGARDograph*, 287, pp. Vol I.

Simpson, R., (1989) "Turbulent boundary layer separation," *Ann. Rev. Fluid Mechanics*, 21, pp. 205–234.

Simpson, R. L., Ghodbane, M., and McGrath, B. E., (1987) "Surface pressure fluctuations in a separating turbulent boundary layer," *Journal of Fluid Mechanics*, 177, pp. 167–186.

Warhaft, Z., (2000) "Passive scalars in turbulent flows," *Ann. Rev. Fluid Mechanics*, 32, pp. 203–240.

Williams, J., (1977) "Incompressible boundary layer separation," *Ann. Rev. Fluid Mechanics*, 9, pp. 113–144.